Grain-Scale Simulation of Shock Initiation in Composite High Explosives

Ryan A. Austin, H. Keo Springer and Laurence E. Fried

Abstract Many of the safety properties of solid energetic materials are related to microstructural features. The mechanisms coupling microstructural features to safety, however, are difficult to directly measure. Grain-scale simulation is a rapidly expanding area which promises to improve our understanding of energetic material safety. In this chapter, we review two approaches to grain-scale simulation. The first is multi-crystal simulations, which emphasize the role of multi-crystal interactions in determining the response of the material. The second is single-crystal simulations, which emphasize a more detailed treatment of the chemical and physical processes underlying energetic material safety.

Keywords Shock initiation · Grain-scale simulation · Strength · Plasticity · HMX · Plastic bonded explosive · Microstructure

1 Introduction

High explosives are materials which release energy upon chemical reaction with sufficient rapidity to produce a supersonic shock wave, called a detonation. Explosive materials come in a wide variety of forms, including granular composites, liquids, suspensions, and gases. Granular composites, however, have the broadest current use in military and industrial applications [1].

In a granular composite explosive, most of the explosive mass is found in a crystalline phase. Some explosive materials are solidified directly from a molten phase [for example, 1,3,5-trinitro-toluene (TNT)] in which case the energetic is a single-phase polycrystal. In other common formulations, a crystalline phase is solidified in a slurry that contains a second crystalline phase with a higher melting

R.A. Austin · H.K. Springer · L.E. Fried (✉)
Lawrence Livermore National Laboratory, Energetic Materials Center, Livermore, CA, USA
e-mail: fried1@llnl.gov

M.K. Shukla et al. (eds.), *Energetic Materials*, Challenges and Advances in Computational Chemistry and Physics 25, DOI 10.1007/978-3-319-59208-4_8

point. A good example of this is the widely used military explosive Composition B, in which TNT is solidified in a slurry containing RDX (1,3,5-trinitroperhydro-1, 3,5-triazine) [1].

One of the most common forms of solid explosive for precision military applications is the plastic bonded explosive (PBX) [2]. Plastic bonded explosives utilize a polymer component to bind crystals of the explosive material together, and may be machined into precision parts. Furthermore, the mechanical properties of a PBX may be dramatically affected by the polymer component (depending on the type and amount of plastic used), allowing for formulations with varying levels of stiffness, strength, and ductility.

The safety properties of high explosive (HE) materials are described by responses to a wide range of insults, including slow impacts, shocks, and heating. One of the most widely studied areas is shock initiation. In the process of shock initiation, a sample is subjected to a shock wave that compresses and heats the material. The explosive responses to shock initiation are typically more repeatable than responses found at lower velocity impacts. Nonetheless, the mechanisms responsible for the shock initiation of solid composites are not understood in detail.

It is known, however, that material defects play an important role in shock initiation [3–5]. When a composite is shocked, the entire material is heated by (bulk) compression. Regions with defects, however, are preferentially heated as compared to non-defective regions of the bulk. These regions of preferential heating are usually referred to as "hot spots". In solid (heterogeneous) explosive materials, there are multiple potential sources of localization that may contribute to temperature rise in the crystalline phase, including, for example, micro-jetting within collapsing pores, inelastic deformation, and frictional sliding along grain surfaces [6]. The mechanisms that are activated under shock wave loading depend on the material of interest, the underlying microstructure, and the rate/intensity of loading.

Although hot spots may occur in many forms, the dominant mechanisms are typically linked to void collapse. When a void collapses, stress-strain work is done on the surrounding material, which produces localized heating. This has been established experimentally by observing changes in shock sensitivity with porosity [7]. Typically, materials with lower porosity are more difficult to shock initiate than materials with higher porosity.

In a typical shock-loaded PBX, the hot spots sizes of interest range from about 0.1–10 μm [8]. These hot spots are formed during the shock rise time ($\sim$1 ns) and may go on to form self-propagating burn fronts or be quenched by heat diffusion on a sub-microsecond time scale. Given the time and length scales that are involved, it has been difficult to resolve the formation and evolution of hot spots by experimental methods. It has therefore been useful to study hot spot dynamics in HE materials via numerical methods (cf. Refs. [9–17] and work cited in Sect. 2). While it is recognized that numerical calculations are not a substitute for experimental observation and measurement, modeling efforts can help to (i) gain insights to the grain-scale behavior, (ii) identify potential material sensitivities, and (iii) develop hypotheses that can be tested in experiments.

There are several possible modeling approaches to grain-scale phenomena in energetic materials [18, 19]. In the following, we describe continuum-based models that have been developed to study hot spot formation at the length scale of (i) individual defects in single crystals, and (ii) crystal aggregates containing many crystals and many defects. Ultimately, we hope that numerical simulations will provide insights to the role of hot spots generated by pore collapse and other defects in HE shock initiation. Such information would be valuable in developing improved macroscopic models of shock initiation and in designing new explosives that are safer than existing materials.

2 Multi-crystal Simulations

Studies to date have mostly focused on the responses of crystal aggregates to shock wave loading. In order to simulate the coupled thermal/mechanical/chemical responses of multiple crystal domains, it is generally necessary to develop simplifications of the underlying physics and chemistry. This has allowed for the study of many-grain interactions and spatial extents that are comparable to the run-to-detonation distances in impact-loaded PBXs. Aggregate simulations are, furthermore, an important part of multi-scale strategies, as they provide information on (non-uniform) hot spot distributions and improved understanding of microstructure-property relationships. As such, this section focuses on the development of multi-crystal/pore simulation frameworks.

The microstructure of a typical PBX is highly heterogeneous. It is composed of crystal/binder phases with potentially disparate thermal/mechanical properties and an assortment of defects (e.g., pores and cracks). An example of a typical micrograph, showing the plastic-bonded explosive PBX-9501, is depicted in Fig. 1 [20]. To resolve hot spot distributions in a shock-loaded PBX, efforts are made to build initial configurations with varying levels of heterogeneity and defect structure. A key challenge associated with these multi-crystal studies is reconstructing realistic instantiations of the HE microstructure.

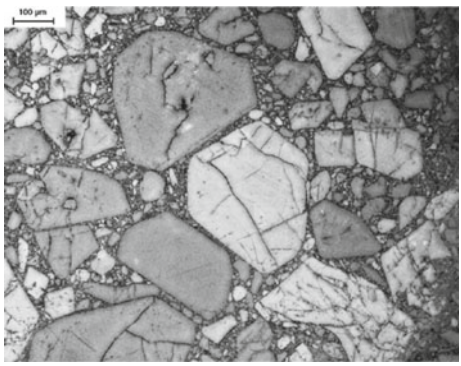

Fig. 1 A micrograph that illustrates the heterogeneous microstructure (grains, binder, internal flaws) of a typical HMX-based plastic bonded explosive, PBX-9501 [20]. The scale marker is 100 μm

2.1 Microstructure Characterization and Reconstruction

The combination of novel explosive microstructure characterization techniques with advances in grain-packing software has allowed for the creation of large, realistic multi-crystal geometries for simulation purposes. In the following, some of the more popular characterization techniques are discussed, including current limitations and trade-offs.

Two-dimensional optical microscopy (cf. Fig. 1) and focused ion beam (FIB) techniques [21] provide highly resolved spatial data (tens of nanometers), which are needed for reconstructing realistic multi-crystal configurations. However, these techniques are destructive and the measurement itself can alter defect populations in the sample of interest. On the other hand, X-ray microtomography (cf. Fig. 2) is a non-destructive technique but resolutions are typically limited to one-thousandth of the field-of-view (e.g., 1 μm for a 1-mm thick sample). This can be insufficient for resolving critical defects when observing representative volume elements. Additionally, a lack of X-ray contrast between the crystal and binder phases can present challenges for resolving grain boundaries. Ultra small angle X-ray scattering [22] can provide information on very small pore structures, ranging from 1 nm to 1 μm, but this technique provides only averaged spatial information.

Grain-packing software tools [23–25] enable either direct initialization of HE composite geometries given suitable microstructural data (e.g., optical or X-ray microtomography data) or reconstruction via reduced sets of microstructure data when spacing or size information is missing (as in the case of ultra small angle X-ray scattering data). In the case of direct initialization, pixel or voxel data is painted onto a mesh. For reduced data sets, particle-packing and tessellation algorithms can be used to generate synthetic microstructures in lieu of explicit geometries.

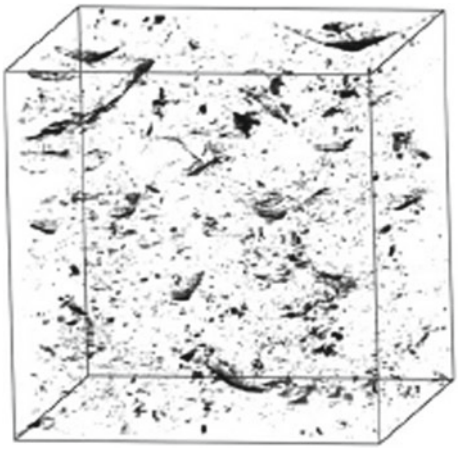

Fig. 2 A typical X-ray microtomography image taken from an HMX-based PBX [74]. The cube size is 0.66 mm and *dark features* are voids

2.2 Survey of HE Shock Initiation Work

The earliest two-dimensional continuum simulations of multiple pore collapse were performed by Mader [26]. These calculations considered a regular array of pores and investigated shock responses both with and without chemical reactions. Despite computational limitations and highly idealized pore geometries, this seminal work demonstrated basic hot spot mechanisms: pore collapse, post-collapse reaction, and stress wave interactions with neighboring pores. Subsequent three-dimensional studies [27, 28] showed that the interactions between multiple collapsing pores is more likely to initiate HE materials, such as nitromethane, HMX, TATB, and PETN, than the collapse of a single pore subjected to the same shock stress.

Benson and Conley [10] considered the dynamic compression of HMX grain aggregates wherein the initial configurations (microstructures) were obtained from digitized experimental micrographs. These calculations were inert and neglected the presence of the polymeric binder. Other studies considered ordered arrays of uniform HMX grains and more-realistic packing structures with non-uniform grain sizes [11, 29]. These calculations showed that the more-realistic microstructures exhibit greater levels of temperature field heterogeneity (cf. Fig. 3) when compared to the case of uniform grain size and spacing.

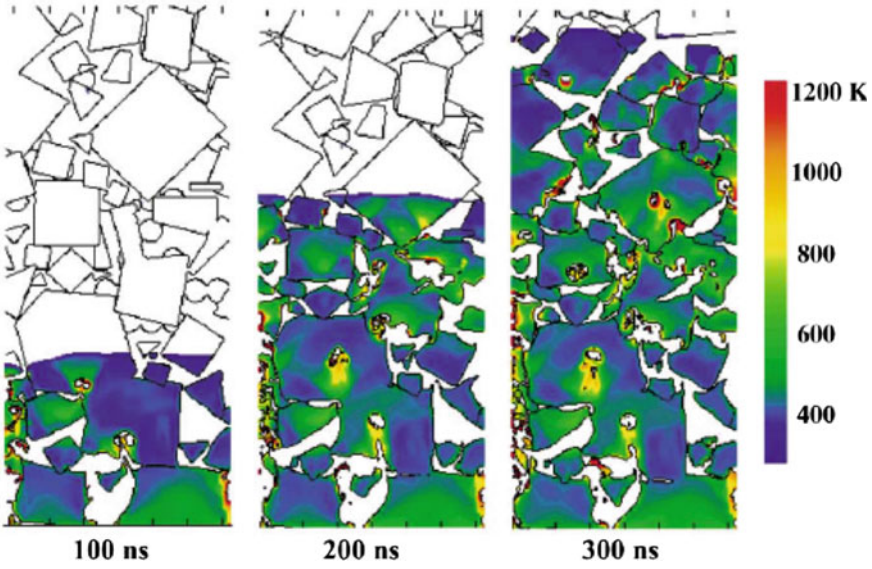

Fig. 3 The computed temperature fields for an HMX-based PBX impacted at 1000 m/s. In these images, the polyurethane binder and void space has been removed for clarity. The localized heating stems from the inelastic work of intergranular pore collapse and material jetting [11]

Cohesive finite element methods have been used to predict the fracture behavior of explosive grains, binder, and interfaces in an HMX-estane PBX subjected to overall strain rates on the order of 10000–100000 s^{-1} [30]. These studies showed that hot spots are formed primarily by viscoelastic heating of the polymeric binder during the early stages of deformation and frictional sliding along crack surfaces at later stages. In Fig. 4, the effects of overall strain rate, energetic volume fraction, and lateral confinement on computed hot spot temperature distribution are illustrated [31]. The temperature of the most frequent hot spots increases with strain rate; this effect is attributed to frictional dissipation. As the energetic volume fraction increases, the average binder thickness decreases and the peak stress increases. This results in earlier fracture and higher frictional dissipation.

Improved Lagrangian calculations employing granular frictional sliding and thermo-elastic-viscoplastic stress-strain response were used to study the compaction of HMX powder beds (85% energetic solid by volume, mean grain size of 60 μm) [32]. In these calculations, it was found that frictional work, not plastic work, is responsible for the highest temperature hot spots at impact speeds of 50–500 m/s. To assess chemical reactivity in these calculations, a critical hot spot size/temperature criterion [8] was evaluated to determine the induction time for various hot spot populations and loading conditions. This criterion was used in a number of other studies as well to establish ignition thresholds for various explosive microstructures [31, 33, 34].

A step forward in realism was achieved in the PBX modeling work of Reaugh [35] (Fig. 5). These simulations were fully three-dimensional, chemically reactive, and incorporated a more realistic description of the polymer/grain/void structure in an HMX-based PBX. From these grain-scale simulation results, a reactive flow macromodel [36] was parameterized to describe the ignition and growth of an assembly of hot spots. In this study, better agreement with detonation velocity data was demonstrated when using a pressure-dependent deflagration model, as compared to a multi-step Arrhenius kinetic, for hot spot growth. This was one of the earliest examples of using multi-crystal calculations to inform a continuum reactive

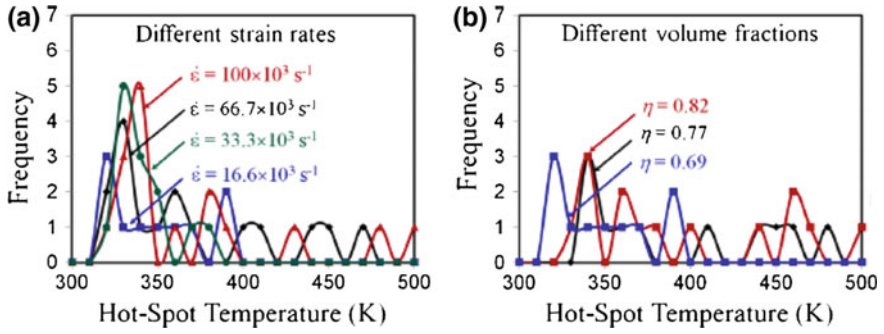

Fig. 4 The simulated effects of (**a**) strain rate and (**b**) energetic volume fraction on hot spot temperature distribution in an HMX-estane PBX under dynamic compression [31]

flow model. Bridging length scales is an important topic that needs to be addressed in future multi-scale studies.

Recent studies have sought to compare short-pulse shock initiation experiments with closely-coupled reactive multi-crystal simulations [16]. In this study, a Kapton flyer (127 μm) impacted LX-10 (95wt% HMX, 5wt% Viton A, 2% porosity) at speeds of 4.3–5.3 km/s. Grain-packing techniques [25] were used to reconstruct microstructures for these simulations, given the composition and grain/pore size distributions, wherein spherical pores were randomly positioned in the LX-10 domain. Porosity was varied from the 2% baseline value to 5, 10, and 20%. Pore radii of 5, 12.5, and 25 μm were used in calculations and resolved using sub-micron zone sizes. A single-step Arrhenius kinetic model [37] was used to describe reactivity. Figure 6 shows that for the baseline porosity of 2%, the relatively smaller, more numerous 5 μm radius pores are more effective at supporting a non-planar reaction front than the large but fewer 25 μm radius pores. The results demonstrate the effects of higher hot spot number density. Figure 7 shows that for a fixed pore radius of 5 μm, the reaction front and overall reaction rate were faster for the 10% porosity case, as compared to the 2% porosity case. At higher porosities, the hot spot density increases and greatly increases the reaction front speed and overall reactivity.

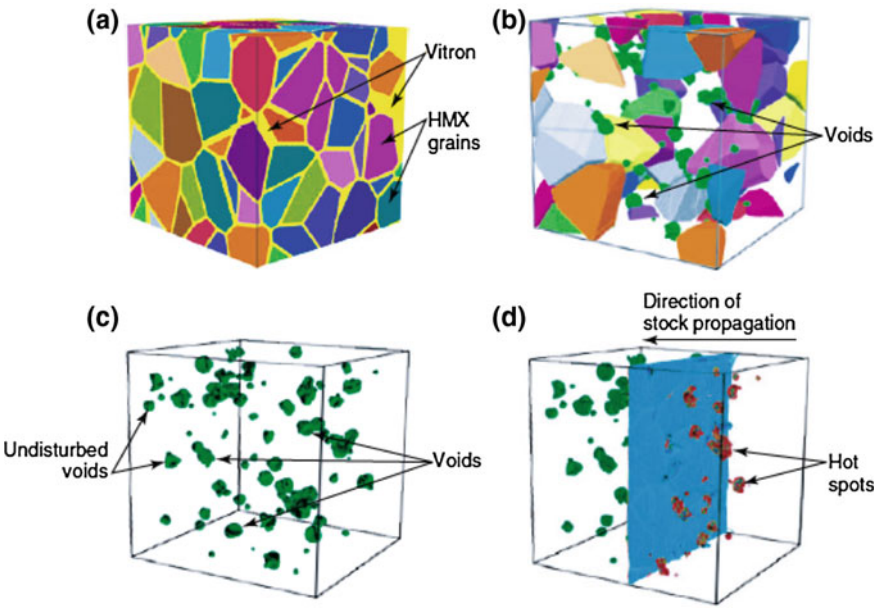

Fig. 5 The formation of hot spots under shock loading in a three-dimensional simulation with detailed microstructures [35]; **a** the faceted HMX grain structure with Viton binder, **b** internal void and grain structure, **c** void structure, and **d** shock wave propagation which induces void closure and hot spot production

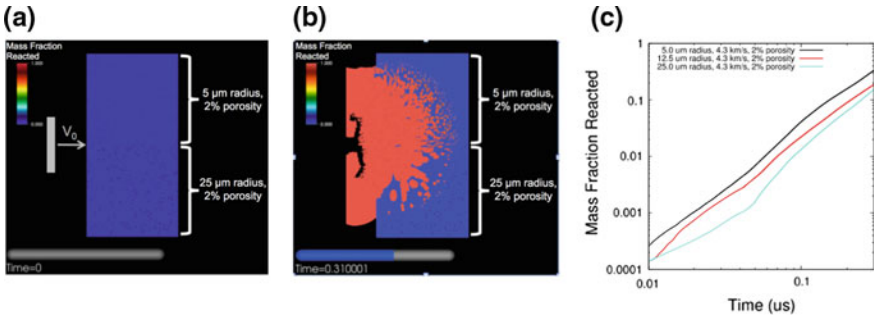

Fig. 6 Calculations of pore size effects (fixed 2% porosity) on non-planar reaction front propagation and overall reactivity of LX-10 impacted by a Kapton flyer (127 μm) at 4.3 km/s: **a** the initial impact conditions with 5 μm radius pores (*top half*) and 25 μm radius pores (*bottom half*), **b** product mass fractions fields, and **c** the time evolution of overall product mass fractions for different pore sizes [16]

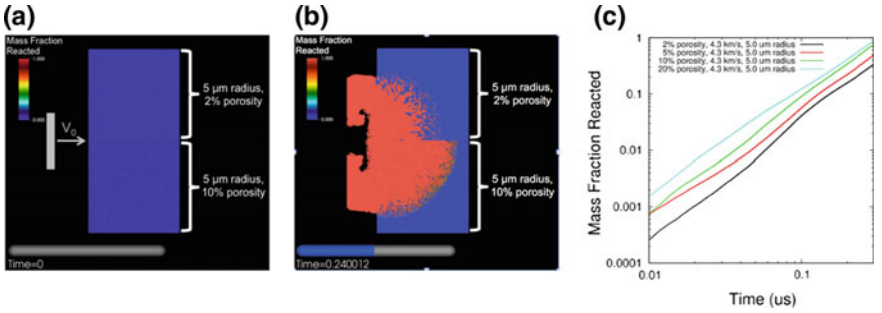

Fig. 7 Calculations of porosity effects (fixed 5 μm radius pores) on non-planar reaction front propagation and the overall reactivity of LX-10 impacted by a Kapton flyer (127 μm) at 4.3 km/s: **a** the initial impact conditions with 2% porosity (*top half*) and 10% porosity (*bottom half*), **b** product mass fraction fields, and **c** the time evolution of overall product mass fractions for 2–20% porosity [16]

Experimental validation of multi-crystal modeling efforts remains a key challenge. To this end, we simulated an HMX powder (1.24 g/cc) subjected to shock loading (1.3 GPa) and compared the calculations to embedded Manganin pressure gauge records [38]. As shown in Fig. 8, the calculations are in rough accord with the pressure gauge records, demonstrating an ability to reproduce run-to-detonation behavior in a multi-crystal simulation framework.

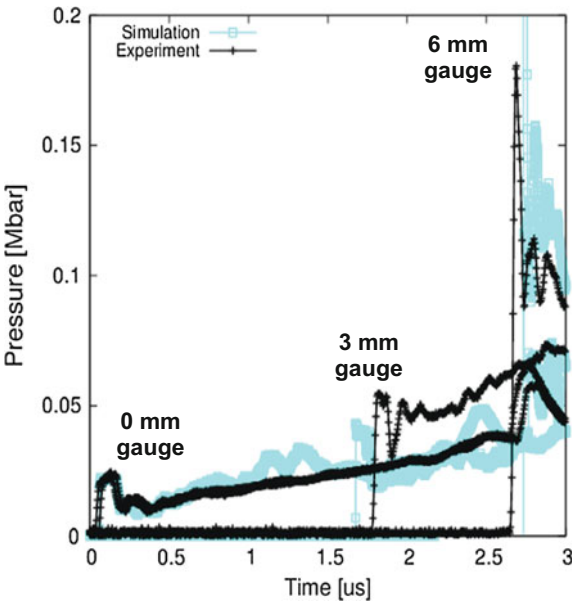

Fig. 8 In-situ pressure records (measured and simulated) from an impacted HMX powder (1.24 g/cc). Detonation is achieved by a run distance of ~6 mm [38]

3 Single-Crystal Simulations

Further insight into the fundamental mechanisms of HE shock initiation can be obtained by considering the collapse of a single pore in a single HE crystal. Although the problem of pore collapse has been considered previously (see, for example, Ref. [12]) we believe continued study is warranted as improved models of grain-scale thermal/mechanical response emerge. In the following, we describe a material model that has been developed for the shock wave loading of HMX. The model is then employed in numerical simulations of pore collapse, with the purpose of investigating energy localization and the mechanisms of shock initiation [39]. The novel aspects of this modeling effort are the treatment of solid-phase strength behavior (a time-dependent anisotropic elastic/plastic formulation is adopted) and thermal decomposition reactions that are driven by the temperature field (i.e., the hot spots). In this regard, it will be shown that the simulated reactivity is sensitivite to the viscoplastic (strength) responses of both the solid and liquid phases. Although we focus on a continuum-based approach here, we would like to note that coarse-grained molecular dynamics [40] or very large scale molecular dynamics [41] are possible alternatives.

3.1 Continuum Model of HMX

The most stable phase of HMX at standard ambient temperature and pressure (298 K, 1 atm) is the crystalline β phase [42, 43]. The β-phase crystal structure is monoclinic, with two molecules per unit cell, as shown in Fig. 9. When porous crystal is subjected to relatively weak shock wave loading, the dissipated energy of inelastic work may be sufficient to melt parts of the crystal phase. At high enough temperatures, the solid and/or liquid phases will undergo decomposition reactions if given enough time. Therefore, the material model described herein addresses two phase transformations: crystal melting ($\beta \rightarrow$ liq) and decomposition reactions that yield gaseous products ($\beta +$ liq $\rightarrow$ gas). The $\beta \rightarrow \delta$ solid phase transformation is ignored, as the loading conditions of interest involve pressures greater than a few GPa [44] and the time scale of interest is short. The $\beta \rightarrow \phi$ transformation that is observed at higher pressures (>27 GPa) [45] is also ignored. In the sections that follow, we provide constitutive relations for the thermal/mechanical behavior of the phases of interest (β, liquid, gas mixture) and an elementary description of the reaction path and kinetics. For a review of HMX properties that have been measured or predicted by computations, one may refer to the literature [46].

3.1.1 Solid Phase

The thermo-elasto-viscoplastic behavior of the β phase is described using a crystal model that was developed in previous work [13]. This model accounts for the anisotropic nature of elastic/plastic deformation and the time-dependence of material flow. A brief account of the crystal model is provided here. The literature should be referenced for full model details and parameterization [13].

Following conventional crystal mechanics treatments, the crystal kinematics are written using a multiplicative decomposition of the deformation gradient tensor, i.e., $\boldsymbol{F} = \boldsymbol{VRF^p}$, where $\boldsymbol{F^p}$ describes the plastic shearing of the lattice, $\boldsymbol{R}$ is the

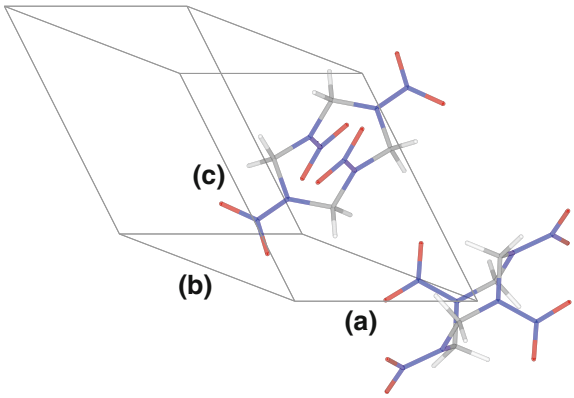

Fig. 9 The unit cell of β-HMX (monoclinic crystal structure) in space group $P2_1/c$. The atoms are colored as: C (*gray*), H (*white*), N (*blue*), O (*red*). The HMX molecules exhibit a chair-like conformation in this phase

lattice rotation, and $\boldsymbol{V}$ is the thermoelastic lattice stretch tensor. In this treatment, plastic deformation is mediated by dislocation motion (crystallographic slip). As such, the velocity gradient in an intermediate configuration is written as,

$$\hat{\boldsymbol{L}} = \dot{\boldsymbol{F}}^{\boldsymbol{p}} \boldsymbol{F}^{\boldsymbol{p}-\mathbf{1}} = \sum \dot{\gamma}^{\alpha} \hat{\boldsymbol{s}}^{\alpha} \otimes \hat{\boldsymbol{m}}^{\alpha} \tag{1}$$

where $\dot{\gamma}^{\alpha}$ denotes the crystallographic shearing rates and $\hat{\mathbf{s}}^{\alpha}$ and $\hat{\mathbf{m}}^{\alpha}$ are unit vectors that define the slip direction and slip plane normal of the αth slip system, respectively. From the Orowan relation,

$$\dot{\gamma}^{\alpha} = \rho_{\perp}^{\alpha} b^{\alpha} \bar{v}^{\alpha} \tag{2}$$

where, with respect to a given slip system, $\rho_{\perp}^{\alpha}$ is the dislocation density, b^{α} is the Burgers vector magnitude, and $\bar{v}^{\alpha}$ is the mean dislocation velocity. The dislocation density is taken as an evolving internal state variable in this description. Constitutive relations have been postulated for the plasticity kinetics (dislocation mobility based on thermal activation and damped glide) and for the evolution of dislocation density [13].

In this work we include the two slip systems that have been experimentally identified, i.e., $(001)[100]$ and $(\bar{1}02)[201]$ in space group $P2_1/c$ [47, 48], and eight additional slip systems that were identified in atomistic calculations [13]. The flow resistance of each slip system scales with the square-root of the total dislocation density (in accordance with the Taylor form). As such, the dislocation density contributes to both the crystal strengthening and the ability to relax non-equilibrium shear stresses via plastic deformation.

The thermoelastic formulation combines the second-order elastic constants [49] with a Murnaghan equation-of-state (EOS) to account for non-linear volumetric response. The EOS parameters were selected to reproduce Hugoniot data from solvent-pressed HMX grain aggregates that are close to fully density [50] and isothermal compression data from diamond anvil cell experiments [45]. It is noted, however, that HMX compressibility data exhibits a wide range of scatter and that recent measurements call into question commonly-accepted parameterizations of the β-HMX EOS [51]. Improving the fidelity of the β-phase EOS is therefore a subject of ongoing work. To allow for melting of the β-phase, an energy-based melting criterion was derived from a Lindemann-type law. The crystal is fully transformed to the liquid phase when the internal energy exceeds the melt energy by an amount equal to the latent heat of melting. The melting behavior is included to account for the loss of static strength in molten regions.

3.1.2 Fluid Phases

The stress-strain responses of the liquid and product gas mixture phases are isotropic. The reference density and EOS of the liquid phase are taken to be identical to that of the β phase. This is assumed purely for expedience and it is recognized that accounting for the actual liquid density and compressibility would improve the model. The volumetric response of each component gas of the product gas mixture is described using a Buckingham exponential-6 potential [52]. The distortional responses of the liquid and gas phases are described using a Newtonian fluid law. In this description, the viscosity is constant (independent of the pressure and temperature). The nominal liquid viscosity is taken as 5.5 cP, which corresponds to the value computed from atomistic simulations performed at 800 K and 1 atm [53]. The gas mixture viscosity is assumed equal to that of the liquid phase for simplicity.

3.1.3 Thermal Properties

The inelastic work done on all phases (β, liquid, gas) is fully dissipated and converted to thermal energy. To compute phase temperatures, it is necessary to have reasonably accurate heat capacities over the temperature range of interest. The heat capacity of the β phase is described using a temperature-dependent Einstein relation, which respects the experimental data at lower temperatures [54] and the classical limit at higher temperatures (i.e., the Dulong-Petit law). The heat capacity of the liquid phase is assumed to be identical to that of the solid phase, for expedience., whereas the heat capacity of gas phase components are described using a set of temperature-dependent polynomials [52]. Thermal expansion effects in the solid and liquid phases are currently neglected.

In non-adiabatic calculations, heat conduction is modeled using Fourier's law. The thermal conductivity of the β phase is assumed to be constant, isotropic, and independent of pressure and temperature. Although analytical predictions suggest that the thermal conductivity tensor of the β phase is close to isotropic [55], refined treatments might incorporate the effects of temperature and pressure on solid-phase thermal conductivity [8, 55]. The thermal conductivities of the liquid and gas phases are assumed to be equal to that of the solid phase, for expedience.

3.1.4 Chemistry

The path and kinetics of decomposition reactions in HMX-based formulations have been investigated in a number of experimental and modeling efforts (cf. Refs. [8, 37, 56–60] and work cited therein). These efforts have focused on reactions initiated by relatively slow direct heating, with samples held under varying levels of confinement. This had led to the construction of a single-step (global) reaction scheme [37] and an assortment of multi-step reaction schemes [8, 37, 61]. However, the reaction path that is followed under shock wave loading has not been identified. In light of this uncertainty, the single-step reaction scheme [37] has been adopted for

its simplicity. The selected reaction addresses the decomposition of both β and liquid-phase HMX, i.e.,

$$\begin{array}{c}\text{HMX}\,(\beta+\text{liquid})\\ C_4H_8N_8O_8\end{array} \rightarrow \begin{array}{c}\text{Product gas mixture}\\ 4\ CO+4\ H_2O+4\ N_2\end{array} \tag{3}$$

In this scheme, the chemical species to be tracked are HMX and the product gas mixture. The kinetics of this reaction are prescribed and handled using the thermochemical code, Cheetah [52]. In addition to the reaction given above, numerous fast reactions are allowed to occur among the product gas components. These reactions, which occur instantaneously, serve to maintain chemical equilibrium among the gas mixture components and the HMX species. As a result, the product gas mixture is adjusted to include other gases (for example, C, H_2, CO_2, HCN, NO_2, etc.). The current product gas composition is therefore not given exactly by (3), but rather that which is obtained by minimizing the Gibbs free energy of system subject to the kinetic constraint on HMX concentration. The species are held in pressure/temperature equilibrium in these calculations. As shown in Table 1, the formation of gaseous products involves a large exothermic heat release, which factors into the model temperature calculations.

The reaction rate law is taken as first-order with respect to the molar concentration of HMX. Therefore,

Table 1 The values of selected material properties and parameters used to model single-crystal HMX shock response

		β-HMX	Liquid-HMX	Product gas mixture
Mass density—ρ_0	g/cm^3	1.904	1.904[a]	–
Molar mass—M	g/mol	296.156	–	–
Bulk modulus—K_0	GPa	15.588	15.588[a]	–
Heat capacity—c_{v0}	J/g-K	0.995	0.995[a]	–
Volumetric CTE—α_0	1/K	0	0	–
Melting temperature—T_{m0}	K	550	–	–
Heat of formation—h_{f0}	J/g	253	489	–4760
Fluid viscosity—η	cP	–	5.5	5.5[b]
Thermal conductivity[c]—κ	W/m-K	0.5	0.5[a]	0.5[b]
Kinetic parameters of decomposition reaction: HMX (β + liquid) → product gas				
Arrhenius frequency factor —k_0	s^{-1}	5.6×10^{12}		
Activation temperature —E_a/R	K	17.9×10^3		

A subscripted zero refers to a property at standard ambient temperature and pressure
[a]Assumed equal to that of the solid phase
[b]Assumed equal to that of the liquid phase
[c]Set to zero in adiabatic simulations

$$\frac{d}{dt}[\mathrm{HMX}] = -\frac{d}{dt}[\mathrm{productgas}] = -k[\mathrm{HMX}] \tag{4}$$

where the rate coefficient, k, displays an Arrhenius-type dependence on temperature. Despite its simplicity, the single-step reaction provides a reasonable approximation of experimentally-measured ignition times when the kinetic parameters of Henson [37] are utilized. As noted above, this formalism assumes the rates of decomposition from the solid and liquid phases are the same. While this seems to be a reasonable starting point, the model might be improved by distinguishing the kinetics of reactions in the solid and liquid phases [57]. Please refer to Table 1 for a partial listing of properties and parameters that are used in the single-crystal simulations.

3.2 Simulations of Intragranular Pore Collapse

The numerical simulations of pore collapse were performed using the multi-physics arbitrary Lagrangian-Eulerian finite element code ALE3D [62]. In this code, the material and mesh are permitted to undergo independent motions, with algorithms accounting for the advection of material among the computational zones (elements). In this way, the mesh is incrementally relaxed over the course of the deformation. This allows for the handling of large strains while avoiding severe mesh distortion.

The computational domain was rendered by locating a single air-filled pore near the center of a rectangular slab of β-HMX crystal. For the time being, work has been limited to 2D plane strain calculations. As such, the idealized flaw is cylindrical in shape. Two-dimensional axisymmetric simulations (for spherical pores) were not considered because the crystal lattice does not display this symmetry. Although full 3D calculations are certainly desirable, we believe such expensive calculations are premature given the developmental state of the material model.

To provide a more realistic description of the microstructure of the crystal phase, the initial dislocation density field is randomly distributed in space (cf. Refs. [13, 39] for details). This is done because the meshing requirements are such that one should expect fluctuations in dislocation density among the elements. The initial field is prescribed such that the initial dislocation density of the full sample is 0.0307 μm^{-2} [13], a value that would be considered typical for annealed metals. A planar shock wave is generated by prescribing the axial component of velocity on the left-hand surface of the crystal slab. The prescribed velocity rises instantaneously, similar to the conditions imposed at the impact face in a plate experiment. The top and bottom surfaces of the crystal sample are periodic and the right-hand

surface is restrained by a rigid frictionless wall. A single shock wave transit of the slab is simulated.

In the following, we examine predictions from the model for various load cases and material modeling assumptions. Of particular interest are the details of deformation localization and the initiation of chemical reactions. With this in mind, we consider the effects of stress wave amplitude, conductive heat transfer, solid-phase flow strength, and liquid-phase viscosity.

3.2.1 Basic Results for a Reference Case

As a reference case, consider a pore diameter of $d = 1\,\mu\text{m}$, an imposed boundary velocity of $u = 1$ μm/ns normal to the $(\bar{1}\bar{1}1)_{P2_1/c}$ plane (this generates a peak axial stress of $\sigma_{11} = 9.4\,\text{GPa}$), and locally adiabatic conditions. For this reference case, a mesh study indicated that 8-nm-zoning was needed for reasonable levels of convergence (cf. Ref. [39]). This amounts to rather fine meshing, as the pore diameter is spanned by 125 elements. To mesh the entire crystal sample $(25d \times 25d)$, about 10 million elements were required. A single pore collapse simulation run in parallel on 512 cores required about 72 h of wall clock time.

To illustrate the basic elements of material response, the pressure and temperature fields for the reference case are given, at three instants in time, in Fig. 10. In this figure, the observation windows are fixed in space and contain only the central portion of the sample. The times given for each snapshot are relative to the time at which the shock front arrives at the left-hand side of the pore. Behind the shock front, the nominal pressure (p) and deviatoric stress (s_{11}) are approximately 6.6 and 2.8 GPa, respectively. The high level of deviatoric stress is due to the rapid compression of the lattice, which produces large (elastic) strains that await relaxation by plastic flow. A release wave is emitted from the crystal-air interface (0.2 ns) as the shock front propagates across the pore. The release wave is followed by a secondary shock that is generated when the pore is fully closed (0.5 ns). This disturbance travels away from the initial pore and beyond the observation window (1.2 ns). The simulations are run until the secondary wave begins to interact with the boundaries, which allows for a post-collapse simulation time of approximately 2 ns.

The localization of deformation and energy is correlated with the development of hot spots in Fig. 10. The temperature fields indicate the formation of a central hot spot around the collapsed pore as well as narrow localization bands that grow away from the pore. These sheets of hot material are shear bands, which are filled with liquid-HMX. The inception and growth of these shear bands is driven by large non-equilibrium shear stresses in the crystal phase. As the shock begins to interact with the pore, the release of material into the pore allows for large shearing deformations in certain locations around the crystal-air interface. The mechanical work is sufficient to melt the crystal in some parts, and the flow strength and viscosity of the liquid phase are much lower than that of the crystal phase. As such,

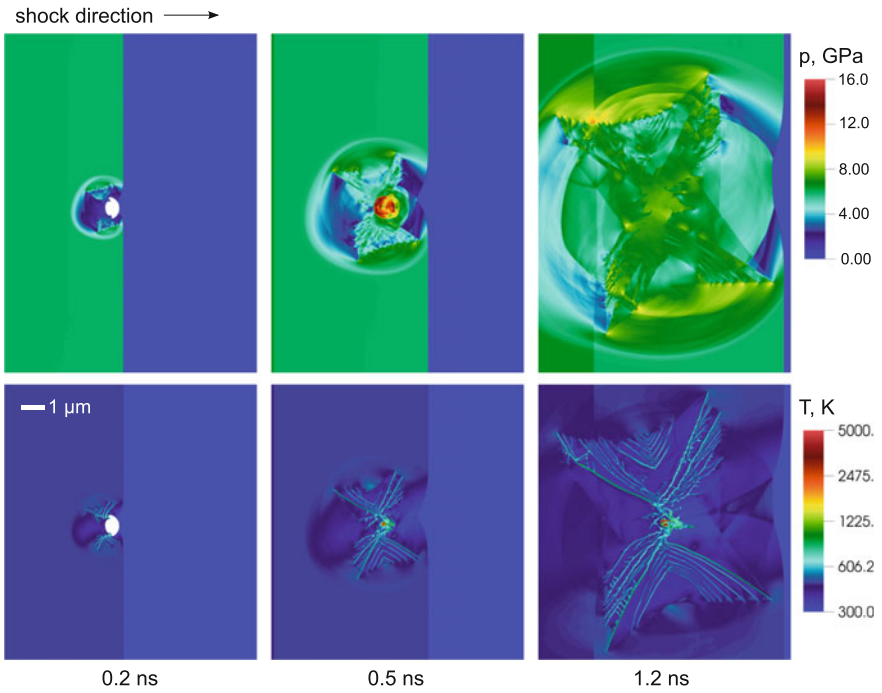

Fig. 10 The pressure and temperature fields that are generated when a shock wave (9.4 GPa) collapses a single pore (1 μm) in β-HMX crystal (reference case simulation parameters). The time origin coincides with the arrival of the shock wave at the left-hand side of the pore [75]

shearing loads that were once supported by the crystal phase are transferred onto the melt band tips and the surrounding material. The ensuing plastic deformation causes continued melting and propagation of bands that are filled with liquid-HMX. The shear bands may therefore be viewed as melt cracks, as the advancement of a band serves to reduce free energy (strain energy of the crystal lattice).

The shear banding (melt cracking) at stress wave amplitudes of 6.5, 9.4, and 10.7 GPa is illustrated in Fig. 11. In this figure, the shear bands are highlighted by plotting the phase fraction of liquid-HMX. At each stress level, a pool of liquid-HMX is formed around the collapsed pore. At 6.5 GPa, a few shear bands grow out of the pore collapse region and branch off to form finer localization bands. When the stress is increased to 9.4 GPa, the shear bands grow in four general directions and exhibit greater amounts of branching. At 10.7 GPa, the spacing of molten sheets is yet finer. In the reference case ($\sigma_{11} = 9.4$ GPa), the shear bands in the lower right-hand quadrant of the crystal sample are approximately 50 nm in width. These bands propagate at a rate of $\sim 4.6\,\mu\text{m/ns}$ and reach temperatures of 500–900 K. The simulated shear banding behavior indicates that the effects of internal flaws (or other material heterogeneities) may not be as localized as one might assume. As shown in Fig. 11, the hot spots generated by the growing shear bands are larger and more extended than

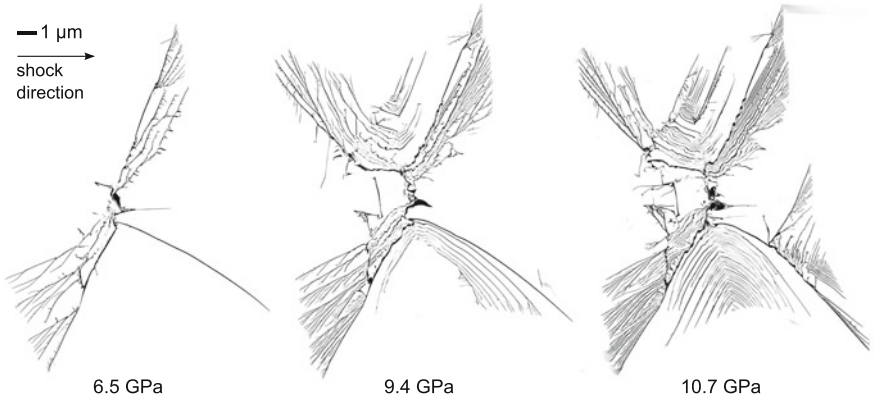

Fig. 11 The shear bands (melt cracks) that are produced when a crystal sample is shock-loaded to different peak stress levels. Here, the phase fraction of liquid-HMX is plotted on a grayscale (ranging from 0 to 1) [75]

the footprint of the original pore. It should be noted that true convergence of localization band behavior (i.e., mesh-independence of results) is not expected unless appropriate provisions are made for dissipative processes, such as heat diffusion or non-local stress-strain response. This should serve as a subject of future work.

Experimental work has documented the tendency of low-symmetry HE crystals to exhibit shear banding under shock wave loading. For example, RDX crystals that were shocked to ~ 13 GPa showed the presence of localization bands and beaded-up volumes of material on the surfaces of recovered samples [63, 64]. The beads are thought to be liquid-RDX that was squeezed out of the localization bands during the shock deformation and which resolidified on the surface of the recovered crystal sample. Shear banding is also predicted in atomistic simulations of shock wave propagation in α-HMX [65] and α-RDX [66]. In the atomistic simulations, the shear banding regions were found to be composed of an amorphous liquid-like phase. These experimental and computational results are encouraging, as this is similar to what is predicted in our continuum β-HMX simulations.

The deformation around the collapsing pore is highly non-uniform, involving the formation and interaction of multiple liquid jets within the pore. For a detailed illustration of the pore collapse process, one may refer to Ref. [39]. In the reference case, material jetting drives up the temperature enough to react a small amount of material in the pore collapse region. The sample reactivity was quantified by product relative mass, $\xi \equiv m_p/m_{pore}$, where m_p is the mass of the product phase and m_{pore} is the "pore mass" (i.e., the reference mass of crystal that would fit inside the initial pore). The reactivity of the low-stress case (6.5 GPa) was quite small on this time scale ($\xi < 0.002$). In the reference case (9.4 GPa), ξ reached a value of ~ 0.08 after a compression time of ~ 2 ns. Increasing the stress to 10.7 GPa did not significantly increase the simulated reactivity. Although the shear bands reach relatively high temperatures (800–900 K), they do not exhibit significant extents of

reaction on this time scale. For higher loads (>20 GPa) such as those observed in short-pulse initiation scenarios, bulk shock melting may occur and bypass localization bands associated with material strength.

We now consider a challenging numerical issue: artificial heat transfer among the species. Since we are employing an ALE method, solution variables need to be advected among the computational zones during the mesh relaxation stage. This numerical advection introduces errors, as solution variables tend to be smeared out in space. For example, if part of a hot (reacted) zone is advected into a neighboring zone that contains cold (unreacted) material, the temperature of the initially cold zone will be uniformly raised due to the mixing of hot and cold volumes. There is not a physical basis for this heat transfer; it is simply an error introduced by the numerical treatment. We attempted to avoid such mixing by shutting off advection in partially reacted zones [39]. This was not successful, however, as the reacting zones experience large volume expansions and require relaxation (advection) to avoid mesh tangling.

Instead of assuming an equilibrated mixture temperature, it may be useful to derive a non-equilibrium treatment that distinguishes the temperatures of the reactant and product species. Mixing among computational zones could then be handled on a species-by-species basis. In this way, when product gas is advected it would only be allowed to mix with other product gas and not serve to heat up the cold unreacted phase. A scheme like this has not yet been employed in our calculations, but should be an objective of future work. The fine zone size (8 nm) that is utilized in these calculations helps to mitigate against artificial heat transfer, as advection errors scale with mesh length. However, there is still some amount of artificial heat transfer among the species, which stems from numerical advection, and this remains an open issue.

3.2.2 Heat Conduction Considerations

The reference case was modeled as adiabatic to generate a baseline response in the absence of physical heat transfer effects. For the time scale considered here, the characteristic dimension of heat diffusion ($\sqrt{\kappa t/\rho c_v}$) is about 20 nm. Although this dimension is small in comparison to the central hot spot (around the collapsed pore), it is non-negligible when compared to the shear band width. Furthermore, the propagation of burn fronts initiated at hot spots depends on heat conduction. It is therefore of interest to assess the dependence of simulation results on assumptions pertaining to heat conduction.

To assess heat transfer effects, the pore collapse simulations were performed with Fourier heat conduction (all other aspects of the reference case remained the same). For a stress wave amplitude of 9.4 GPa, the temperature field that was

computed with heat conduction was rather similar to that computed using the adiabatic model [39]. The temperature gradients were, of course, less steep in the conductive case, but the central hot spots were of similar size and temperature. Peak temperatures in the shear bands were reduced by up to $\sim 100\,\mathrm{K}$. The flux of heat away from the central hot spot renders the conductive case slightly less reactive than the adiabatic case. For example, the computed extent of reaction (ξ) was reduced by less than 10% [39]. This indicates that the adiabatic assumption is reasonable when the simulation duration is limited to a few nanoseconds, as the results of interest are not changed in a substantial way when heat conduction is included. However, simulations that seek to address longer time scales (e.g., tens to hundreds of nanoseconds) and hot spot burning should treat heat conduction in a meaningful way.

We would like to note that the (macroscopic) Fourier law breaks down when the length scale of interest approaches the mean free path of the phonons. Since the pore collapse calculations involve strong temperature gradients over tens of nanometers, we believe it will be important to adopt a more sophisticated treatment of small-scale heat transfer. For example, one that accounts for phonon interactions [67].

3.2.3 Model Sensitivity to Solid Flow Strength

We now consider the dependence of simulation results on the flow strength of the solid phase. The crystal model, which has been used in all simulations up to this point, accounts for the elastic/plastic anisotropy of the β phase and the time-dependent nature of plastic deformation. The time- or rate-dependence of plasticity is thought to be important here because many solids exhibit a sharp increase in flow stress at higher rates. In regard to the problem of pore collapse, if the time scale of plastic relaxation is comparable to the time scale of pore collapse, high shear stresses will persist until they are relieved by inelastic deformation. These shear stresses factor into the mechanical work, which is responsible for a large fraction of the temperature rise.

To investigate effects related to solid flow strength, a pore collapse simulation was performed using a conventional isotropic/rate-independent strength model for the β phase. Here, the yield strength is taken as $Y = Y_0(1 + \beta\varepsilon^p)^n$, where Y_0 is the initial yield strength, ε^p is the effective plastic strain (a proxy for internal state), and β and n are hardening parameters. In the literature, it has been common to assume a constant yield strength in the range of 0.060–0.180 GPa [10, 11, 68]. To consider the effects of somewhat higher strength and weak strain-hardening behavior, the following parameters were selected: $Y_0 = 0.300\,\mathrm{GPa}$, $\beta = 0.060$, $n = 1$. All other aspects of the reference-case simulation remained the same.

The temperature fields that are computed from the isotropic/rate-independent model are shown in Fig. 12. The pore is now collapsed by a single smooth jet that produces a symmetric configuration of two hot spots. The appearance of these hot

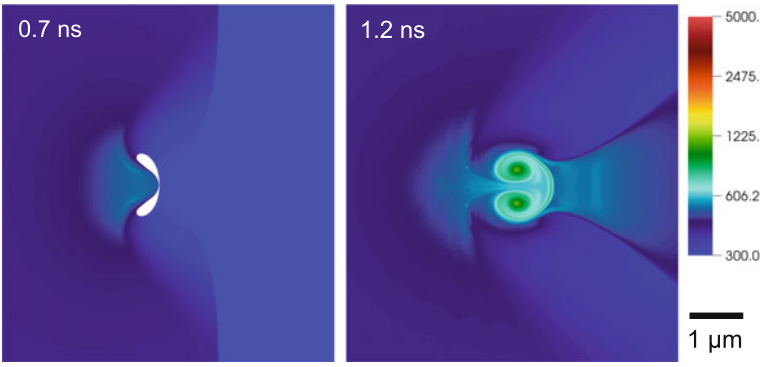

Fig. 12 The temperature fields that are obtained when pore collapse is simulated using a rate-independent/isotropic strength model (reference case simulation parameters, otherwise). The closure process and degree of localization are in sharp contrast to predictions from the rate-dependent/crystal model [75]

spots is largely due to vortical flows that are set up on either side of the impinging jet. These temperature fields may be compared to those computed earlier using the crystal model (Fig. 10). In the rate-dependent/crystal calculations, shear banding is a prominent feature of the deformation. In the rate-independent/isotropic calculations, energy localization is confined to the immediate surroundings of the pore and there is no shear banding.

The differences in localization behavior are largely attributed to the strain-rate-dependence of the strength model. Although rate-dependent flow stresses are often seen as tending to suppress localization (given that higher stresses are required to drive higher strain rates), this notion breaks down in the presence of thermal softening and melting. Such is the case in our rate-dependent calculations, where relatively large flow stresses and small plastic strains are sufficient to melt the material located at the tips of the localization bands. In the rate-independent case, the stress state is forced to remain on a strain-rate-independent yield surface and plastic strains are computed according to a consistency condition. For the parameters chosen above, the mechanical work is insufficient to trigger shear banding. It may be possible to induce shear banding in the rate-independent model by prescribing a higher yield strength. This, however, would be at odds with experimental stress-strain curves at quasistatic rates [69] and the observed relaxation behavior under shock wave loading [48]. It is, however, possible to induce shear banding by assigning sufficient strain-rate-dependence to an isotropic model. In this case, the bands form on the planes of maximum shear, whereas, in the crystal model, the details of plastic flow and band structuring are sensitive to the slip plane orientations.

To quantify the differences in thermal energy localization predicted by these models, temperature histograms were computed near the end of the simulation (cf. Fig. 13). These histograms were constructed by binning the sample mass according

to temperature and normalizing those bins by the pore mass. As shown in Fig. 13, the isotropic model is biased toward lower temperatures (notice the large peak in-between 400 and 500 K), whereas the crystal model predicts higher temperatures due to shear localization (600–1200 K) and exothermic reaction (>2000 K). For equivalent energies imparted to each sample, the crystal model predicts higher degrees of localization and, therefore, hot spots that are larger or higher in temperature. The extent of reaction that is predicted by the rate-independent model is effectively zero on this time scale, despite the formation of hot spot temperatures of greater than 1000 K. Therefore, the solid-phase strength law has a significant effect on the character of shock-induced plasticity, the peak temperatures that are generated, and the initiation of reactions due to pore collapse.

3.2.4 Model Sensitivity to Liquid Viscosity

The localization bands that grow out of the pore collapse region are filled with liquid-HMX (cf. Fig. 11). In this model, the liquid phase is treated as a simple Newtonian fluid. Although the viscosity of the liquid phase is expected to depend on the pressure and temperature (and perhaps strain rate as well), we assumed that the liquid viscosity is constant for the sake of simplicity. In the reference case, the liquid viscosity was taken as 5.5 cP, corresponding to the atomistic value at 800 K and 1 atm [53]. We now consider the sensitivity of the model to the assumed liquid viscosity. As a comparative case, the liquid viscosity was increased to 22.0 cP, which corresponds to the atomistic value at 700 K. All other aspects of the reference case remained the same.

The temperature field that is obtained when pore collapse is simulated using the higher liquid viscosity is given in Fig. 14. The shear bands are now wider, fewer in number, and hotter than those of the lower-viscosity case (Fig. 10). The shear band temperatures are higher in this case because of greater mechanical dissipation within the bands. The temperatures within the shear bands are now high enough to

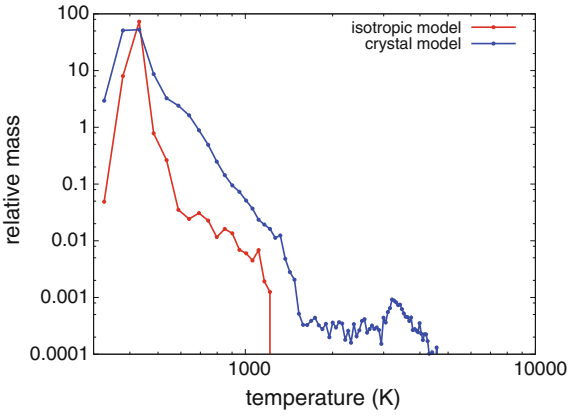

Fig. 13 The temperature histograms that are computed (in log-log space) when pore collapse is simulated using a rate-independent/isotropic strength model and the rate-dependent/crystal model [75]

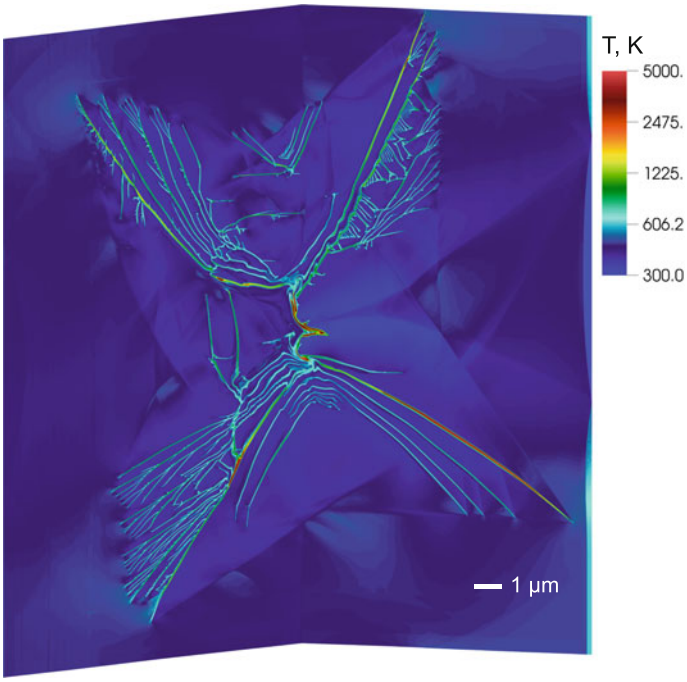

Fig. 14 The temperature field computed for the case of higher liquid viscosity (22.0 cP). Reactions now occur in both the central hot spot (pore collapse region) and the shear bands, due to increased mechanical dissipation [75]

drive decomposition reactions on this time scale (see, for example, the forward-most band in the lower right-hand quadrant of Fig. 14).

To illustrate sample reactivity, time histories of product relative mass (ξ) were computed for the lower- and higher-viscosity cases (cf. Fig. 15). The initial trajectory of the product curve is controlled by reactions that occur in the liquid phase around the central hot spot (pore collapse region). In the reference case, reactions are confined to the central hot spot, with roughly 10% of the pore mass reacted after a few nanoseconds. The higher-viscosity case exhibits higher reactivity from the start, due to increased mechanical dissipation around the central hot spot. At about 2 ns, however, the higher-viscosity case exhibits a sharp increase in overall reaction rate. This corresponds to the onset of chemical reactions in the shear bands. During a post-collapse simulation time of ~ 2 ns, ξ reaches a value of ~ 0.8. The appearance of rapidly-growing, reactive shear bands suggest that the initiation of HE crystals, such as HMX, may be dominated by planar burn waves emitted from localization bands, rather than spherical burn fronts from more compact sources.

The model predictions of reactivity are therefore quite sensitive to the viscosity of the liquid phase. This is because the liquid within a band can be subjected to exceptionally high shearing rates. Since the liquid phase experiences temperatures

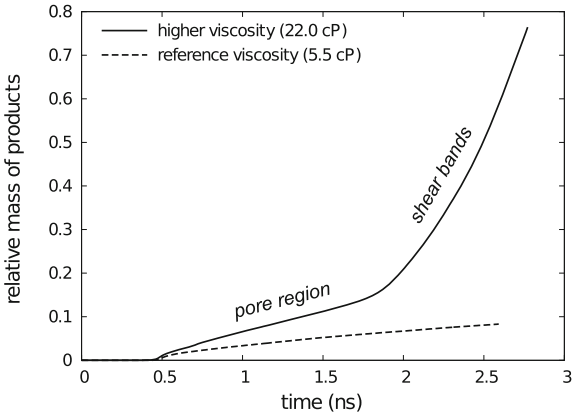

Fig. 15 The product curves computed for lower and higher liquid viscosities. The sharp increase in reaction rate for the higher-viscosity case is due to the onset of reactions in the shear bands [75]

ranging from about 550 K (initial melting at 1 atm) to greater than 1000 K, future modeling efforts should incorporate the temperature-dependent liquid viscosity that was computed in atomistic simulations, i.e., $\eta = \eta_0 \exp(T_a/T)$, where $\eta_0 = 3.1 \times 10^{-4}$ cP and $T_a = 7800\,\mathrm{K}$ [53]. The effect of pressure on liquid viscosity should also be considered, although we are not aware of any such data.

4 Concluding Remarks

The development of models for the grain-scale behavior of HE materials under dynamic loading conditions is an area of long-standing interest. Such efforts are needed to help elucidate the mechanisms of impact-induced hot spot formation and reaction initiation and should be viewed as complementary to experimental investigations, which are challenging to perform at the time/length scales of interest. Along these lines, we are enthusiastic about new ultra-fast measurement techniques that have been developed to probe the shock compression of HE crystals on sub-ns time scales [51]. These are truly grain-scale type measurements that may be used to further assess and refine the single-crystal model of Sect. 3 in the near future.

This article focused on the development of HE models at two length scales: (i) a coarser scale, which considers the shock responses of crystal aggregates with many defects/heterogeneities, and (ii) a finer scale, which considers single-crystal response and the behavior around a single defect (pore). In the latter, we described a continuum model that was developed for the thermal/mechanical/chemical responses of HMX. This model was used to simulate pore collapse in shock-loaded β-phase crystal and attendant energy localization modes. The single-crystal pore collapse results indicate: (i) a modest extent of reaction is achieved when an adiabatic reference case ($d = 1\,\mu\mathrm{m}$) is shock-loaded up to $\sim 10\,\mathrm{GPa}$ and held for a few nanoseconds; (ii) the growth of shear bands is an important mode of localization;

(iii) hot spot dissipation via heat conduction is an important consideration for compressions longer than a few nanoseconds; (iv) the strain-rate-dependence of solid-phase strength behavior has a strong bearing on energy localization; and (v) the reactivity of impact-induced shear bands (melt cracks) is sensitive to the viscosity of the liquid phase.

Although the crystal model represents a step forward in realism, much remains to be done to improve the fidelity of model predictions. For example, the HMX material model would be improved by a better treatment of melting and liquid-phase behavior. In this regard, one might include kinetics for the $\beta \rightarrow$ liquid phase transformation, a more appropriate description of the liquid-phase EOS (i.e., one that is distinct from the solid phase), distinct kinetics for (faster) decompositions from the liquid phase [57], and a liquid phase viscosity that depends on pressure and temperature, as the simulated reactivity is quite sensitive to this property. Formulations that treat non-equilibrium species temperatures (within a given material point, or computational cell) may also prove valuable for mitigating against artificial heat transfer in various numerical settings.

The overall spatial extents that can be handled using the single-crystal model are obviously limited. To reach larger volume elements, which better reflect the heterogeneity of actual PBX microstructures, it is useful to consider aggregate calculations that employ coarsened descriptions of constituent behavior. Establishing a link between the single-crystal calculations and multi-crystal models (for example, by some information passing scheme) remains a major objective of ongoing work. A next step would then involve coarse-graining multi-crystal (aggregate) responses to obtain a PBX macromodel. However, much remains to be done to establish these connections.

Looking ahead, there are several long-standing questions for which the multi-crystal (aggregate) simulations may provide insight:

- How does defect size, spacing, morphology, and orientation influence hot spot formation and growth under shock loading conditions?
- What are the bounds on defect size that produce hot spots that are relevant to the shock initiation process?
- How does defect location in the explosive/binder system influence shock initiation behavior? For example, intragranular defects versus interfacial defects vs. binder defects.
- How does non-uniform binder coating thickness and explosive/binder impedance mismatch influence shock initiation behavior?
- How does explosive/binder microstructure and constituent properties (adhesion, flows strength) influence fragmentation, which is important to reaction violence in safety scenarios?

Such efforts must proceed with some level of experimental validation at appropriate time/length scales and this remains a major outstanding challenge.

In closing, we would like to note that multi-scale strategies that merge descriptions coming from the fine/intermediate length scales may provide a basis

for developing new PBX macromodels that incorporate microstructure-property information and, therefore, improve upon existing hot spot models [70–73]. We believe such microstructure-aware models would be valuable in designing high explosive materials for specific applications with tailored performance and safety.

Acknowledgements This work was performed under the auspices of the U.S. Department of Energy by Lawrence Livermore National Laboratory under Contract DE-AC52-07NA27344 (LLNL-BOOK-692711).

References

1. Köhler J, Meyer R (1993) Explosives, fourth edition. VCH, Weinheim, FRG
2. Teipel U (2005) Energetic materials: particle processing and characterization. Wiley-VCH, Weinheim, FRG
3. Bowden FP, Yoffe AD (1952) Ignition and growth of explosions in liquids and solids. Cambridge University Press, UK
4. Campbell AW, Davis WC, Ramsay JB, Travis JR (1961) Shock initiation of solid explosives. Phys Fluids 4(4):511–521
5. Field JE, Swallowe GM, Heavens SN (1982) Ignition mechanisms of explosives during mechanical deformation. Proc Roy Soc Lond A Mat 382(1782):231–244
6. Field JE (1992) Hot spot ignition mechanisms for explosives. Acc Chem Res 25(11):489–496
7. Garcia F, Vandersall KS, Tarver CM (2014) Shock initiation experiments with ignition and growth modeling on low density HMX. J Phys: Conf Ser 500:052048
8. Tarver Craig M, Chidester Steven K, Nichols Albert L (1996) Critical conditions for impact- and shock-induced hot spots in solid explosives. J Phys Chem 100:5794–5799
9. Charles L Mader (1997) Numerical modeling of explosives and propellants. CRC press, USA
10. Benson DJ, Conley P (1999) Eulerian finite-element simulations of experimentally acquired HMX microstructures. Modell Simul Mater Sci Eng 7:333–354
11. Baer MR (2002) Modeling heterogeneous energetic materials at the mesoscale. Thermochim Acta 384:351–367
12. Menikoff R (2004) Pore collapse and hot spots in HMX. Proc APS Topical Group Shock Compression Condens Matter 706:393–396
13. Barton Nathan R, Winter Nicholas W, Reaugh John E (2009) Defect evolution and pore collapse in crystalline energetic materials. Modell Simul Mater Sci Eng 17:035003
14. Najjar FM, Howard WM, Fried LE, Manaa MR, Nichols A III, Levesque G (2012) Computational study of 3-D hot spot initiation in shocked insensitive high-explosive. Proc APS Topical Group Shock Compression Condens Matter 1426:255–258
15. Kapahi A, Udaykumar HS (2013) Dynamics of void collapse in shocked energetic materials: physics of void–void interactions. Shock Waves 23(6):537–558
16. Springer HK, Tarver CM, Reaugh JE, May CM (2014) Investigating short-pulse shock initiation in HMX-based explosives with reactive meso-scale simulations. J Phys: Conf Ser 500:052041
17. Kapahi A, Udaykumar HS (2015) Three-dimensional simulations of dynamics of void collapse in energetic materials. Shock Waves 25(2):177–187
18. Rice BM (2012) Multiscale modeling of energetic material response: Easy to say, hard to do. Shock Compression Condens Matter—2011, Parts 1 and 2 1426:1241–1246
19. Brennan JK, Lisal M, Moore JD, Izvekov S, Schweigert IV, Larentzos JP (2014) Coarse-grain model simulations of non-equilibrium dynamics in heterogeneous materials. J Phys Chem Lett 5:2144–2149

20. Skidmore CB, Phillips DS, Howe PM, Mang JT, Romero AJ (1999) The evolution of microstructural changes in pressed HMX explosives. In: 11th international detonation symposium, p 556
21. Wixom RR, Tappan AS, Brundage AL, Knepper R, Ritchey MB, Michael JR, Rye MJ (2010) Characterization of pore morphology in molecular crystal explosives by focused ion beam nanotomography. J Mater Res 25(7):1362
22. Willey TM, van Buuren T, Lee JR, Overturf GE, Kinney JH, Handly J, Weeks BL, Ilavsky J (2006) Changes in pore size distribution upon thermal cycling of TATB-based explosives measured by ultra-small angle X-ray scattering. Prop, Explos, Pyrotech 31(6):466
23. Torquato S (2002) Random heterogeneous materials: microstructure and macroscopic properties. Springer, New York
24. Kumar NC (2008) Reconstruction of periodic unit cells of multimodal random particulate composites using genetic algorithms. Comp Mater Sci 42:352
25. ParticlePack Friedman G, Manual User (2015) Version 3:1
26. Mader C L. The two-dimensional hydrodynamic hot spot, volume IV. *Los Alamos National Laboratory Technical Report*, LA-3771, 1967
27. Mader CL, Kershner JD (1967) Three-dimensional modeling of shock initiation of heterogeneous explosives. In: 19th International Combustion Symposium, p 685
28. Mader CL, Kershner JD (1985) The three-dimensional hydrodynamic hot-spot model. In: 8th International Detonation Symposium, p 42
29. Baer MR, Kipp ME, van Swol F (1999) Micromechanical modeling of heterogeneous energetic materials. In: International detonation symposium, p 788
30. Barua A, Zhou M (2011) A Lagrangian framework for analyzing microstructural level response of polymer-bonded explosives. Model Simul Mater Sci Eng 19:055001
31. Barua A, Horie Y, Zhou M (2012) Energy localization in HMX-estane polymer-bonded explosives during impact loading. J Appl Phys 111(5):054902
32. Panchadhara R, Gonthier KA (2011) Mesoscale analysis of volumetric and surface dissipation in granular explosive induced by uniaxial deformation waves. Shock Waves 21:43
33. Barua A, Kim S, Horie Y, Zhou M (2013) Ignition criteria for heterogeneous energetic materials based on hotspot size-temperature threshold. J Appl Phys 113:064906
34. Kim S, Barua A, Horie Y, Zhou M (2014) Ignition probability of polymer-bonded explosives accounting for multiple sources of material stochasticity. J Appl Phys 115(17):174902
35. Reaugh JE (2002) Grain-scale dynamics in explosives. Technical Report UCRL-ID-150388-2002, Lawrence Livermore National Laboratory
36. Lee EL, Tarver CM (1980) Phenomenological model of shock initiation in heterogeneous explosives. Phys Fluids 23(12):2362–2372
37. Henson BF, Asay BW, Smilowitz LB, Dickson PM (2001) Ignition chemistry in HMX from thermal explosion to detonation. Technical report LA-UR-01-3499, Los Alamos National Laboratory
38. Springer HK, Vandersall KS, Tarver CM, Souers PC (2015) Investigating shock initiation and detonation in powder HMX with reactive mesoscale simulations. In: 15th International detonation symposium
39. Ryan AA, Nathan RB, John ER, Laurence EF (2015) Direct numerical simulation of shear localization and decomposition reactions in shock-loaded HMX crystal. J Appl Phys 117 (18):185902
40. Moore JD, Barnes BC, Izvekov S, Lisal M, Sellers MS, Taylor DE (2016) A coarse-grain force field for RDX: density dependent and energy conserving. J Chem Phys 144(10):104501
41. Tzu-Ray S, Aidan PT (2014) Shock-induced hotspot formation and chemical reaction initiation in PETN containing a spherical void. J Phys: Conf Ser 500:172009
42. Cady HH, Larson AC, Cromer DT (1963) The crystal structure of alpha-HMX and a refinement of the structure of beta-HMX. Acta Cryst 16:617–623
43. Chang SC, Henry PB (1970) A study of the crystal structure of-cyclotetramethylene tetranitramine by neutron diffraction. Acta Cryst. B., 26(9):1235–1240, 1970

44. Elizabeth AG, Joseph MZ, Alan KB (2009) Pressure-dependent decomposition kinetics of the energetic material HMX up to 3.6 GPa. J Phys Chem A 113(48):13548–13555
45. Choong-Shik Y, Hyunchae C (1999) Equation of state, phase transition, decomposition of β-HMX (octahydro-1, 3, 5, 7-tetranitro-1, 3, 5, 7-tetrazocine) at high pressures. J Chem Phys 111(22):10229–10235
46. Ralph M, Thomas DS (2002) Constituent properties of HMX needed for mesoscale simulations. Combust Theor Model 6(1):103–125
47. Sheen DB, Sherwood JN, Gallagher HG, Littlejohn AH, Pearson A (1993) An investigation of mechanically induced lattice defects in energetic materials. Technical report, Final Report to the US Office of Naval Research
48. Dick JJ, Hooks DE, Menikoff R, Martinez AR (2004) Elastic-plastic wave profiles in cyclotetramethylene tetranitramine crystals. J Appl Phys 96(1):374–379
49. Thomas DS, Ralph M, Dmitry B, Grant DS (2003) A molecular dynamics simulation study of elastic properties of HMX. J Chem Phys 119(14):7417–7426
50. Marsh SP (1980) LASL Shock Hugoniot data. University of California Press, Berkeley, CA
51. Zaug JM, Armstrong MR, Crowhurst JC, Ferranti L, Swan R, Gross R, Teslich Jr NE, Wall MA, Austin RA, Fried LE (2014) Ultrafast dynamic response of single crystal PETN and beta-HMX. In: 15th international detonation symposium
52. Laurence EF, Howard WH (1998) An accurate equation of state for the exponential-6 fluid applied to dense supercritical nitrogen. J Chem Phys 109(17):7338–7348
53. Dmitry B, Grant DS, Thomas DS (2000) Temperature-dependent shear viscosity coefficient of octahydro-1, 3, 5, 7-tetranitro-1, 3, 5, 7-tetrazocine (HMX): a molecular dynamics simulation study. J Chem Phys 112(16):7203–7208
54. Baytos JF (1979) Specific heat and thermal conductivity of explosives, mixtures, and plastic-bonded explosives determined experimentally. Technical report LA-8034-MS, Los Alamos Scientific Laboratory
55. Long Y, Liu YG, Nie FD, Chen J (2012) A method to calculate the thermal conductivity of HMX under high pressure. Philos Mag 92(8):1023–1045
56. John Z, Rogers RN (1962) Thermal initiation of explosives. J Phys Chem 66(12):2646–2653
57. Rogers RN (1972) Differential scanning calorimetric determination of kinetics constants of systems that melt with decomposition. Thermochim Acta 3(6):437–447
58. McGuire RR, Tarver CM (1981) Chemical-decomposition models for the thermal explosion of confined HMX, TATB, RDX, and TNT explosives. In Proceedings of the 7th international detonation symposium, pp 56–64
59. Craig MT, Tri DT (2004) Thermal decomposition models for HMX-based plastic bonded explosives. Combust Flame 137(1):50–62
60. Jack JY, Matthew AM, Jon LM, Albert LN, Craig MT (2006) Simulating thermal explosion of octahydrotetranitrotetrazine-based explosives: model comparison with experiment. J Appl Phys 100(7):073515
61. Aaron PW, William MH, Alan KB, Albert LN III (2008) An LX-10 kinetic model calibrated using simulations of multiple small-scale thermal safety tests. J Phys Chem A 112(38):9005–9011
62. Albert LN (2007) ALE-3D user's manual
63. Coffey CS, Sharma J (2001) Lattice softening and failure in severely deformed molecular crystals. J Appl Phys 89(9):4797–4802
64. Sharma J, Armstrong RW, Elban WL, Coffey CS, Sandusky HW (2001) Nanofractography of shocked RDX explosive crystals with atomic force microscopy. Appl Phys Lett 78(4):457–459
65. Jamarillo E, Sewell TD, Strachan A (2007) Atomic-level view of inelastic deformation in a shock loaded molecular crystal. Phys Rev B 76:064112
66. Cawkwell MJ, Thomas DS, Lianqing Z, Donald LT (2008) Shock-induced shear bands in an energetic molecular crystal: application of shock-front absorbing boundary conditions to molecular dynamics simulations. Phys Rev B 78(1):014107
67. Minnich AJ (2015) Advances in the measurement and computation of thermal phonon transport properties. J Phys: Condens Matter 27(5):053202

68. Harry KS, Elizabeth AG, John ER, James K, Jon LM, Mark LE, William TB, John PB, Jennifer LJ, Tracy JV (2012) Mesoscale modeling of deflagration-induced deconsolidation in polymer-bonded explosives. In Proceedings of the APS topical group on shock compression of condensed matter, vol 1426, p 705
69. Rae PJ, Hooks DE, Liu C (2006) The stress versus strain response of single β-HMX crystals in quasi-static compression. In Proceeding of the 13th international detonation symposium, p 293–300
70. Kang J, Butler PB, Baer MR (1992) A thermomechanical analysis of hot spot formation in condensed-phase, energetic materials. Combust Flame 89:117
71. Massoni J, Saurel R, Baudin G, Demol G (1999) A mechanistic model for shock initiation of solid explosives. Phys Fl 11:710
72. Nichols III AL, Tarver CM (2003) A statistical hot spot reactive flow model for shock initiation and detonation of solid high explosives. 12th Int Det Symp 489
73. Nichols AL III (2006) Statistical hot spot model for explosive detonation. AIP Conf Proc 845:465
74. Willey TM, Lauderbach L, Gagliardi F, van Buuren T, Glascoe EA, Tringe JW, Lee JR, Springer HK, Ilavsky J (2015) Mesoscale evolution of voids and microstructural changes in HMX-based explosives during heating through β–δ phase transition. *J. Appl. Phys.*, 118:055901, 2015
75. Reproduced with permission from Austin RA, Barton NR, Reaugh JE, Fried LE J Appl Phys 117:185902. Copyright 2015, AIP Publishing LLC